IJMMM International Journal of Minerals, Metallurgy and Materials 矿物冶金与材料学报（英文版）

Microstructural evolution during the progressive transformation-induced plasticity effect in a Fe–0.1C–5Mn medium manganese steel

Mei Zhang, Wenhao Li, Yangfei Chen, Yang Jiang, Xiaofei Guo, and Han Dong

Cite this article as:
Mei Zhang, Wenhao Li, Yangfei Chen, Yang Jiang, Xiaofei Guo, and Han Dong, Microstructural evolution during the progressive transformation-induced plasticity effect in a Fe–0.1C–5Mn medium manganese steel, *Int. J. Miner. Metall. Mater.*, 32(2025), No. 2, pp. 369-379. https://doi.org/10.1007/s12613-024-2963-z

View the article online at SpringerLink or IJMMM Webpage.

INTERNATIONAL JOURNAL OF
Minerals, Metallurgy and Materials

Volume 32, Number 2, February 2025
Page 369

Research Article https://doi.org/10.1007/s12613-024-2963-z

Microstructural evolution during the progressive transformation-induced plasticity effect in a Fe–0.1C–5Mn medium manganese steel

Mei Zhang[1,2),✉], *Wenhao Li*[1)], *Yangfei Chen*[1)], *Yang Jiang*[1)], *Xiaofei Guo*[1,2),✉], *and Han Dong*[1,2),✉]

1) School of Materials Science and Engineering, Shanghai University, Shanghai 200444, China
2) State Key Laboratory of Advanced Special Steel, Shanghai University, Shanghai 200444, China
(Received: 30 April 2024; revised: 25 June 2024; accepted: 28 June 2024)

Abstract: The microstructural evolution of a cold-rolled and intercritical annealed medium-Mn steel (Fe–0.10C–5Mn) was investigated during uniaxial tensile testing. *In-situ* observations under scanning electron microscopy, transmission electron microscopy, and X-ray diffraction analysis were conducted to characterize the progressive transformation-induced plasticity process and associated fracture initiation mechanisms. These findings were discussed with the local strain measurements via digital image correlation. The results indicated that Lüders band formation in the steel was limited to 1.5% strain, which was mainly due to the early-stage martensitic phase transformation of a very small amount of the less stable large-sized retained austenite (RA), which led to localized stress concentrations and strain hardening and further retardation of yielding. The small-sized RA exhibited high stability and progressively transformed into martensite and contributed to a stably extended Portevin–Le Chatelier effect. The volume fraction of RA gradually decreased from 26.8% to 8.2% prior to fracture. In the late deformation stage, fracture initiation primarily occurred at the austenite/martensite and ferrite/martensite interfaces and the ferrite phase.

Keywords: medium-Mn steel; retained austenite; progressive transformation-induced plasticity effect; local strain; fracture initiation

1. Introduction

Given the demand for automotive steel with high strength and excellent impact energy absorption capacity, medium manganese steel (MMnS) has become attractive candidates for automotive sheet-forming applications [1–3]. MMnS achieves an ultrafine and multiphase microstructure through cold rolling (CR) and intercritical annealing (IA) processes in the ferrite–austenite two-phase region [4–7]. A certain amount of austenite shows stability at room temperature (RT), but it can transform into martensite during deformation and remain preserved in the microstructure. The volume fraction and stability of the retained austenite (RA) play vital roles in controlling the strength, ductility, and work-hardening capability of MMnS [8–11]. Hu *et al.* [12] proposed a multi-alloyed design principle together with a direct intercritical rolling process to obtain RA with high content and optimal stability and provided persistent transformation-induced plasticity (TRIP) effect on work hardening and damage resistance. A detailed description of the specific behavior of RA during the deformation process is currently unavailable. Therefore, in terms of size and morphology, the effect of the progressive TRIP process, particularly the influence of the RA, on strain hardening and fracture initiation behavior throughout the entire deformation process must be understood.

The formation of Lüders band and Portevin–Le Chatelier (PLC) bands during the tensile deformation of MMnS shows an association with localized deformation in banded structures [13–18]. Lüders strain, which typically exceeds 5% strain [19–20], negatively affects the application of CR MMnS. Wang *et al.* [21] observed that the optimization of CR reduction in IA MMnS is an effective means of reducing Lüders strain. Li *et al.* [22] limited Lüders strain through prestraining, which resulted in the increased average stability of the RA; as a result, the occurrence of the TRIP effect was delayed, and the initiation strain of Lüders bands was suppressed. Although these methods effectively reduced Lüders strain through suppression of the TRIP effect during yielding, they can also reduce plasticity. Furthermore, the formation of PLC bands leads to uneven deformation and early necking, although it increases the strength of steel [14]. Revealing the microstructural evolution under the effect of progressive TRIP will help in elucidating the mechanisms of fracture initiation.

The microstructural evolution of a MMnS (Fe–0.1C–5Mn) was investigated at various stages of tensile deformation during *in-situ* tensile test under scanning electron microscopy (SEM). Transmission electron microscopy (TEM) and X-ray diffraction (XRD) were used to characterize the micro-

✉ Corresponding authors: Mei Zhang E-mail: zmei@shu.edu.cn; Xiaofei Guo E-mail: xiaofei_guo@shu.edu.cn;
Han Dong E-mail: 13910077790@163.com

Springer

structural features and volume fracture of RA, respectively. The austenite stability and the associated progressive TRIP effect during tensile deformation are discussed in detail.

2. Experimental

The investigated MMnS, which was denoted as Fe–0.1C–5Mn, had a chemical composition of 0.10wt% C, 4.96wt% Mn, and 0.04wt% Al. The material was heated to 800°C (slightly above the Ac3 temperature of 740°C) and quenched in water to RT to obtain a predominantly martensitic microstructure. Subsequently, the microstructure was subjected to IA at 625°C for 12 h and air-cooled to RT.

Tensile specimens with a gauge length of 50 mm and width of 12.5 mm were machined parallel to the rolling direction (RD). A MTS C45.305 tensile testing machine was used to conduct uniaxial tensile tests at RT at a crosshead speed of 3 mm/min, which is equivalent to a nominal strain rate of 1×10^{-3} s^{-1}. Digital image correlation (DIC) analysis was performed using the GOM system with ARAMIS v6.3.0 image processing software [23]. Prior to the tensile test, the specimen surfaces were sprayed with scattered spots. Strain distribution during tensile deformation was analyzed.

The microstructural evolution at different strain stages was observed during *in-situ* tensile tests under an Apollo 300 field-emission scanning electron microscope. Tensile specimens with a gauge length of 11 mm and width of 2 mm were polished in accordance with the standard metallographic procedure and corroded with a 4vol% nitric acid in alcohol (Nital) solution. *In-situ* tensile tests with interrupted electro-back scattering diffraction (EBSD) characterization were performed using a Thermo Scientific Scios 2 scanning electron microscope and Oxford instrument EBSD detector (step size 0.06 μm). The specimens had a gauge length and width of 2 mm and 1.5 mm, respectively. Surface preparation was achieved through electropolishing in a mixed solution of 90% alcohol and 10% perchloric acid. A JEM-2010F transmission electron microscope was used to reveal the microstructure substructures at an acceleration voltage of 200 kV. The specimens were cut into 3 mm-diameter thin foils, ground to a 50 μm thickness, and electropolished with a solution of 5vol% perchloric acid in alcohol at −30°C using a twin-jet machine.

The volume fraction of RA was determined using a D/Max 2500 XRD system with a Cu K_α radiation source operated at 40 kV and 250 mA and a scanning speed of 1°/min. The material was electropolished in a solution containing 10vol% perchloric acid and 90vol% ethanol for the preparation of XRD samples [12]. The integrated intensities of (200)α, (211)α, (200)γ, (220)γ, and (311)γ diffraction peaks were analyzed using Eq. (1) to calculate the volume fraction of RA:

$$V_\gamma = 1.4I_\gamma/(I_\alpha + 1.4I_\gamma) \quad (1)$$

where V_γ indicates the volume fraction of the RA, I_γ denotes the integrated intensity of the austenite peaks, and I_α refers to the integrated intensity of the ferrite peaks [24–25]. The austenite consumption with an increased strain can be described using Eq. (2):

$$f_\gamma/f_0 = \exp(-k\varepsilon) \quad (2)$$

where f_0 represents the original RA volume fraction, f_γ corresponds to the RA volume fraction at a given strain ε, k represents the mechanical stability of RA, and ε denotes deformation strain [26].

3. Results

3.1. Mechanical properties

Fig. 1 reveals the engineering and true stress–strain curves of the Fe–0.1C–5Mn steel. The steel exhibited a yield strength (YS) of 510 MPa with an evident yield platform and an ultimate tensile strength (UTS) of 775 MPa. In addition, the steel demonstrated a uniform elongation (UE) of around 35%, with a total elongation (TE) of 40%. Remarkably, the steel exhibited excellent strength and ductility exceeding 30 GPa·%, which substantially surpassed that of first-generation advanced high-strength steels [27]. Furthermore, a ~1% Lüders strain, along with indications of a PLC effect at the late deformation stage, was revealed by fluctuations in the magnified images [28]. The magnified image in Fig. 1(b) highlights a distinct work-hardening zone between the true strains of 0.15 and 0.25, and this outcome is usually associ-

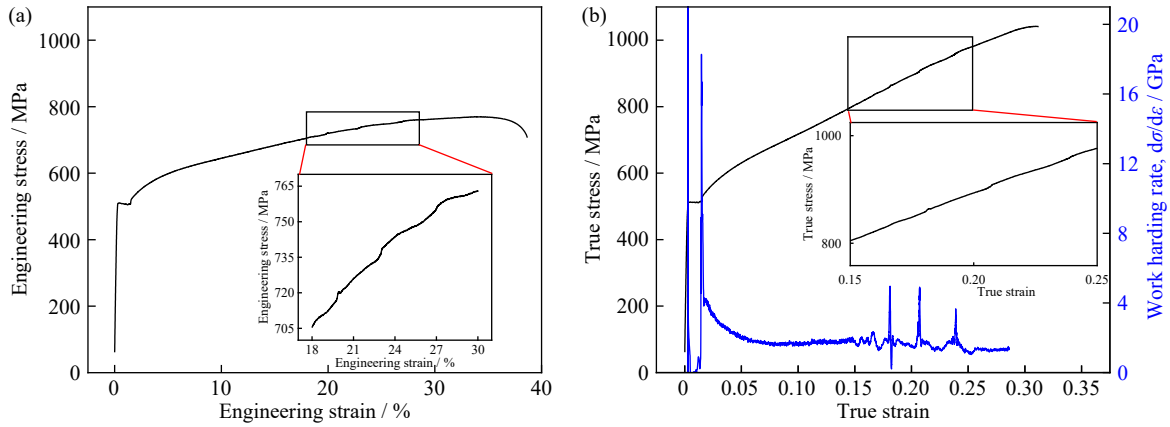

Fig. 1. (a) Engineering stress–strain curve and (b) true stress–strain curve and work hardening rate–strain curve of the Fe–0.1C–5Mn steel.

ated with deformation-induced martensitic transformation [16].

3.2. Strain distribution

The DIC analysis revealed a mesoscopic local strain (LS) distribution during tensile deformation. Fig. 2 displays the distribution of the von Mises strain in the early deformation stages (1%–3% global strain (GS)). At 1% GS, an uneven strain distribution was observed, and it was accompanied by the presence of Lüders bands across the gauge length, which corresponded to the yield platform. This finding was due to the dislocations pinned by the carbon atoms and formed a Cottrell atmosphere. With the increase in the external force, dislocations broke free from the Cottrell atmosphere and showed continued movement. As the stress dropped to a lower yield point, the Lüders bands diffused along the length of the specimen (2%–3% GS). After yielding, strain inhomogeneities were minimized (Fig. 2(b)).

Fig. 3 displays the LS distribution between the 6%–40% GS. The major strain distribution map and curve revealed uniform deformation of the material until 33% GS. However, noticeable fluctuations in LS occurred in the major strain curves between 13% and 33% GS. Beyond 33% GS, the peak LS increased to 50% at 38% GS, which indicates the onset of necking. Ultimately, the tensile specimen fractured with the peak LS exceeding 80% at 40% GS.

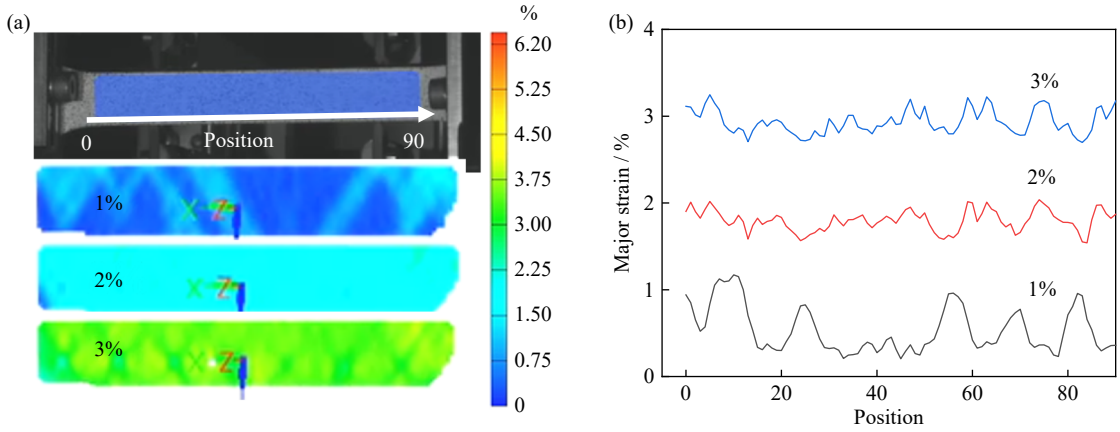

Fig. 2. LS distribution of the Fe–0.1C–5Mn steel at early tensile deformation stages (1%–3% GS): (a) major strain distribution map; (b) major strain as a function of position.

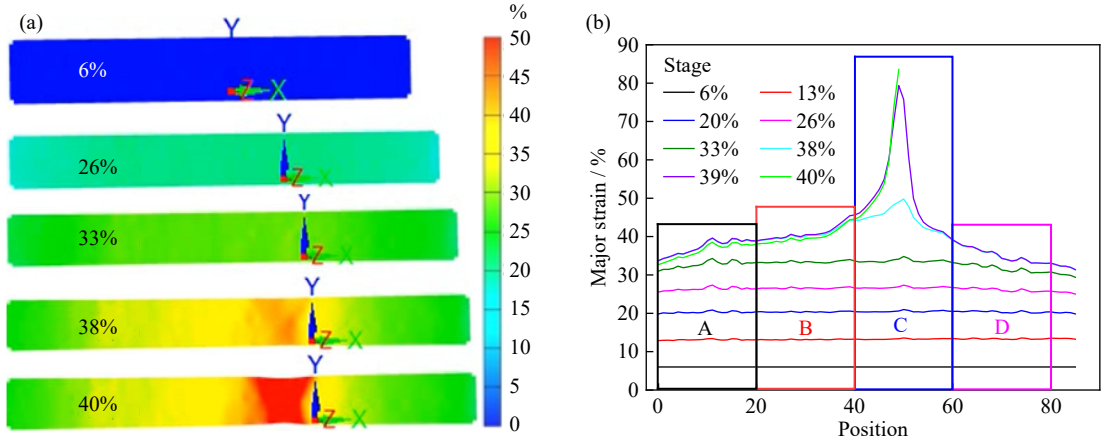

Fig. 3. Strain distribution of the Fe–0.1C–5Mn steel during the tensile process (6%–40% GS): (a) major strain distribution map; (b) major strain as a function of position.

3.3. Microstructural evolution during tensile deformation

Fig. 4 shows the *in-situ* tensile deformation under SEM characterized via interrupted EBSD used to trace local phase transformation, grain re-orientation, and strain localization at the micrometer level during the tensile process. Fig. 4(a1) displays the tensile stress–displacement curve. The normalized deformation strain for interrupted EBSD characterization was calculated through comparison with the quasistatic tensile curve in Fig. 1(a) and indicated beneath each characterization point. Fig. 4(b1) presents the phase distribution map of the undeformed state of the material, which featured 77.4% ferrite with an average grain size of ±2.7 μm and 8.0% RA with an average grain size of ±0.3 μm. The RA showed a discontinuous distribution along grain boundaries and a large variation in grain size. The phase distribution maps in Fig. 4(b1)–(f1) revealed the initial disappearance of larger RA grains during the tensile process. At the strain of 18.2%, a portion of RA with a small grain size remained, which indicates its high stability. Within the low-deformation range

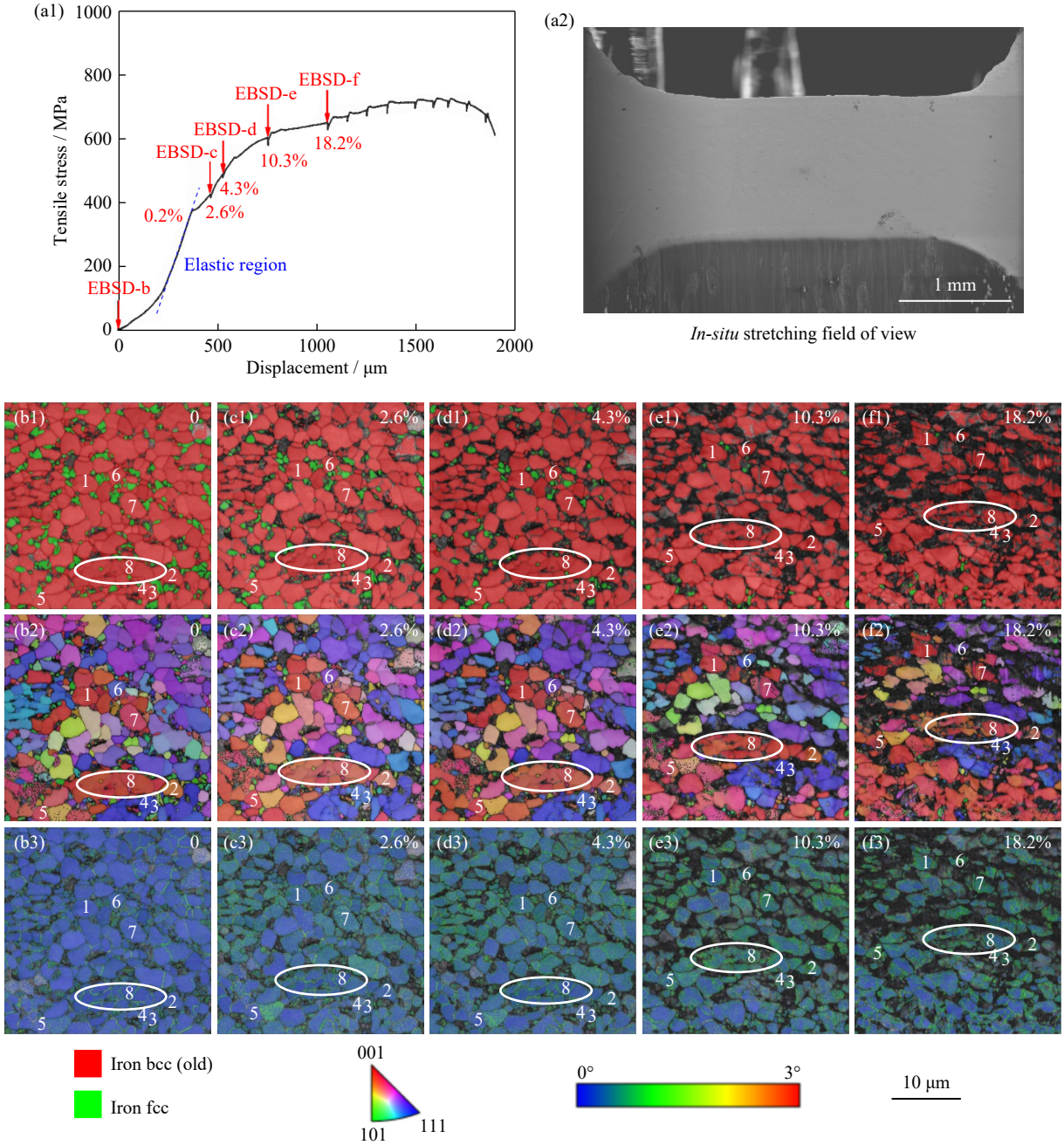

Fig. 4. ***In-situ*** **tensile test of the Fe–0.1C–5Mn steel under SEM with interrupted EBSD characterization at different strains: (a1) tensile stress–displacement curve; (a2)** ***in-situ*** **stretching field of view; (b1–f1) phase distribution maps; (b2–f2) inverse pole figures; (b3–f3) kernel average misorientation maps.**

(Fig. 4(c1)–(c3) and (d1)–(d3)) with a normalized strain of 2.6%–4.3%, the microstructure features showed no significant changes. When the displacement reached 750 μm (Fig. 4(e1)–(e3)), which corresponded to a deformation strain of ~10.3%, a large amount of RA disappeared and transformed into martensite (Fig. 4(e1)).

The characteristic ferrite grains (marked with 1–8, represented F1–F8) were selected based on the surrounding status of RA. As shown in Fig. 4(b1), ferrite grain F1 was surrounded by a number of larger austenite grains. By contrast, the austenite surrounding grains F6–F8 is dispersed and in small size. They exhibited different deformation and crack initiation behaviors during tensile deformation. As depicted by the horizontal width of grain in Fig. 4(b1)–(f1), ferrite grain F1 did not exhibit considerable deformation throughout the tensile process, with its horizontal width increasing slowly from 3.6 μm (Fig. 4(b1)) to 3.7 μm at 18.2% strain (Fig. 4(f1)). As shown in Fig. 4(b3)–(e3), grain F1 exhibited low kernel average misorientation (KAM) values throughout the tensile process. The RA surrounding grain F1 showed a higher strain concentration, which was indicated by the raised KAM values when the strain was increased from 0 to 18.2%. At the strain of 18.2%, the resolution around grain F1 was lost, probably due to its high dislocation density. F1 grain revealed strain localization near the grain boundaries (KAM value (0.8° ± 0.1°)), and by comparison, the interior had

KAM values of (0.2° ± 0.1°).

For the ferrite grain with surrounding small-sized RA, such as grain F6, coupled with anchorage by small-sized ferrite, its coordinated deformation was restricted such that its horizontal width increased slowly from 2.3 μm (Fig. 4(b1)) to 2.7 μm (Fig. 4(e1)) at 10.3% strain. Similarly, ferrite grain cluster F8 was anchored by small-sized austenite, with its horizontal width gradually increasing from 12.1 to 13 μm at 10.3% strain. At 18.2% strain (Fig. 4(f1)), grains F2–F8 revealed initiated cracks at interfaces, and the majority of the RA was assumed to have transformed into martensite, which could not further raise the plasticity through the TRIP effect. The remaining small-sized RA remained stable as its small size supported its high stability against phase transformation.

In addition, ferrite grains F2, F5, and F7 experienced fracture, and their sizes remained relatively unchanged. By contrast, F3, F4, and F6 revealed significant deformation. The inverse pole figure map in Fig. 4(b2)–(f2) reveals that the grain orientation of F2, F5, and F7 is (001)//RD, while F3, F4, and F6 exhibit (111)//RD orientation. For grains with a body-centered cubic structure, grains with (001)//RD orientation will experience more difficulty in promoting the dislocation slip needed for coordinated deformation [29]. This finding is also a potential explanation for the splitting of the F7 grain at 9.3% deformation strain, although it was surrounded by fewer large-sized RA, which can increase plasticity through TRIP transformation. As revealed by the KAM in Fig. 4(e3) and 4(f3), the split ferrite grains F2–F7 had relatively higher KAM values, which indicates a considerable strain localization.

Fig. 5 displays the second electronic image of the microstructure at the GS of 0, 1.5% (yielding point elongation: YPE), 10%, 20%, 30%, and 40% (fracture), respectively. Initially, the undeformed Fe–0.1C–5Mn steel comprised fine ferrite grains (~2 μm measured by Image J®), equiaxed austenite, and a martensite/austenite two-phase structure (Fig. 5(a)). The austenite grains were distinguished from the ferrite or martensite phase through measurement of the Mn content using an energy dispersive spectrometer (EDS). As reported by Gibbs *et al.* [26] the austenite with Mn content lower than 10% resulted in only α′-martensite transformation, and α′ and ε martensite developed between 10% and 15% Mn, respectively; an austenitic mixture formed when the Mn content exceeded 15%. Between 0 and 20% GS, notable changes were absent in the microstructural features, except for the uniaxial elongation of ferrite grains and transformation of individual large RA. When the GS was raised from 0 to 40% (Fig. 5(a) and (f)), the horizontal length of ferritic grain A (F_A) and ferritic grain B (F_B) raised from 1.56 and 2.00 μm to 3.33 and 2.58 μm, respectively. The plasticity was partly provided by the ferrite grains, as soft ferrite grains exhibited better formability and lower YS than austenite grains. The size of the ferrite measured via ImageJ showed around 80% LS of partial ferrite after fracture, and the ferrite with a low-deformation level attained a strain exceeding 30%. The surface became undulated, and partial small-grain austenite transformed into martensite after 20% GS (Fig. 5(e)). The stress–strain curve in Fig. 1(a) reveals the serrated flow at 20%–30% elongation. As revealed in Fig. 3(b), the LS intensified at several positions when the GS exceeds 20%, while the necking occurred in the C region as the GS exceeds 33%, which signifies a substantial phase transformation from austenite to martensite. However, small-sized austenite with a submicrometer grain size did not undergo transformation until fracture. This finding suggests that RA with high stability in this zone did not obtain sufficient mechanical free energy to transform into martensite. The strain of austenite was approximately 18%, which is considerably smaller than that of ferrite. However, the volume expansion caused by γ→α′ transformation led to plastic deformation of the surrounding ferrite matrix, which resulted in the rise in the dislocation density that hardened the material. With the further increase in strain, the voids gradually developed into cracks. Meanwhile, voids formed at large-sized and transformed austenite/ferrite grain boundaries (Fig. 5(e)) grew during further tension, as shown in Fig. 5(f)).

Fig. 6 presents the microscopic morphology at a spot of 2 mm away from the fracture surface before deformation and deformed with 40% GS, where considerably less pronounced changes in microstructure were observed compared with those near the fracture surface. This difference was attributed to the LS concentration near the fracture zone reaching ~80% major strain, whereas the LS concentration was ~40% in the region of uniform deformation.

The volume fractions of RA in the interrupted tensile test specimens were measured by XRD in the uniform deformation regions, as displayed in Fig. 7. The diffraction pattern in Fig. 7(a) reveals the presence of a small amount of ε-martensite between 20% and 30% GS. The peaks of ε-martensite disappeared near the fracture surface, which indicates that the ε-martensite subsequently transformed into α′-martensite. Fig. 7(b) shows the calculated volume fraction of RA at different deformation strains derived from XRD measurements. The material initially had an RA volume fraction of 26.8%. At 1% GS, the volume fraction of the RA decreased to 26.4%, but it subsequently decreased with the increase in GS. This finding follows the relationship described by Eq. (3), which was obtained through parameter fitting as per Eq. (2).

$$f_\gamma = 0.268 \exp(-2.91\varepsilon) \tag{3}$$

At 40% GS, the volume fraction of RA reduced to 8.2%, which accounted for a 69.4% reduction compared with the initial RA. For comparison, an XRD measurement point close to the fracture surface was determined, with a yield of an RA of 4.1%. The region near the fracture surface exhibited a higher LS due to necking behavior, which was expected to further improve the RA-to-martensite transformation.

Fig. 8 displays the bright-field TEM image of undeformed Fe–0.1C–5Mn steel. Fig. 8(a) shows the relatively dislocation-free ferrite phase in undeformed conditions [30]. The austenite can be distinctly distinguished from ferrite by selected area electron diffraction (SAED). The findings re-

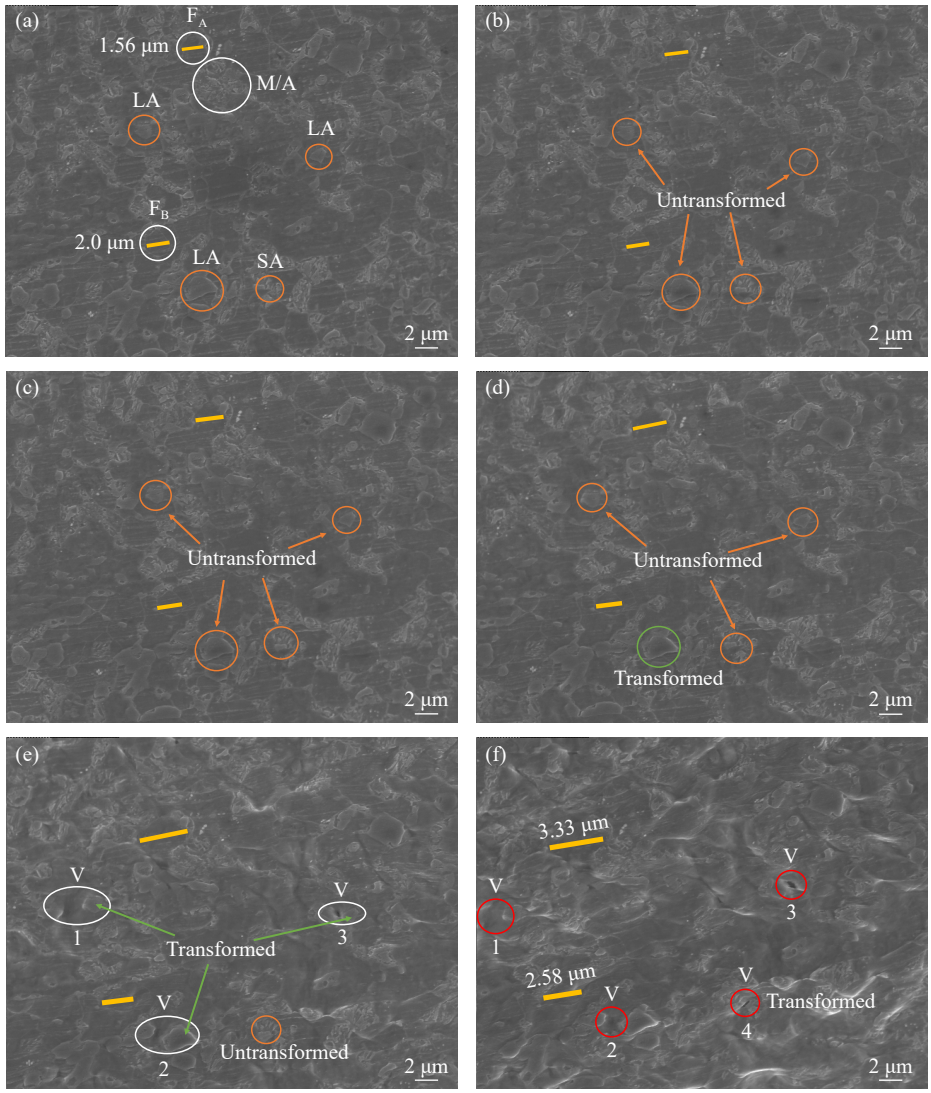

Fig. 5. SEM images obtained at different strains of *in-situ* tensile specimens of Fe–0.1C–5Mn steel: (a) 0, (b) 1.5% (yielding); (c) 10%, (d) 20%, (e) 30%, and (f) 40% (fracture surface). F—Ferrite; A—Austenite; M—α′-Martensite; LA—Large-sized austenite; SA—Small-sized austenite; V—Void.

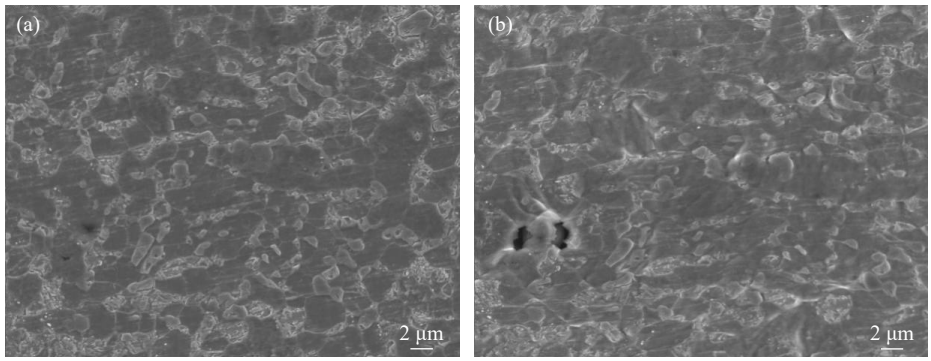

Fig. 6. SEM images at the spot with a 2 mm distance from the fracture surface: (a) 0 and (b) 40% GS.

veal large-sized (around 2 μm in length) and small-sized (below 1 μm in length) austenite islands. Lath martensite and less frequent recrystallization twins were distinctly observed in some partial large-sized austenite islands (Fig. 8(b)).

Fig. 9 displays the bright-field TEM micrographs of the Fe–0.1C–5Mn steel deformed by 10% deformation strain. Fig. 9(a) shows that α′-martensite was also detected in small-sized austenite, although at low amounts [30]. Steineder *et al.* [31] reported that lath-like martensite promotes dislocation interaction and deformation cell formation. Fewer dislocations were observed in fresh martensite (Fig. 9(b)), while a large number of dislocation lines, dislocation walls, and dislocation tangles were observed in ferrite grains (Fig. 9(c)).

Fig. 10 reveals the dark-field TEM images of the Fe–0.1C–5Mn steel subjected to a 30% deformation strain. Stacking faults (SFs) and ε-martensite enriched in large-sized

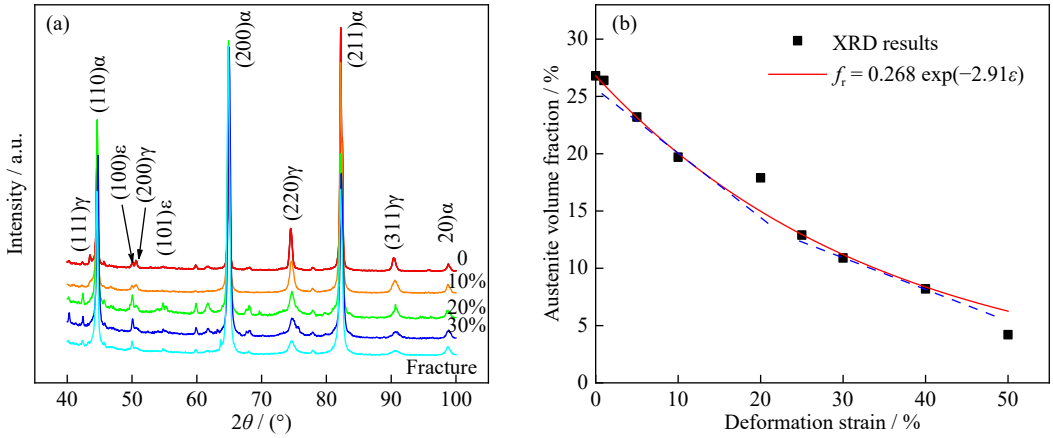

Fig. 7. XRD measurement in interrupted tensile specimens at different strains: (a) diffraction pattern; (b) volume fraction of RA as a function of deformation strain.

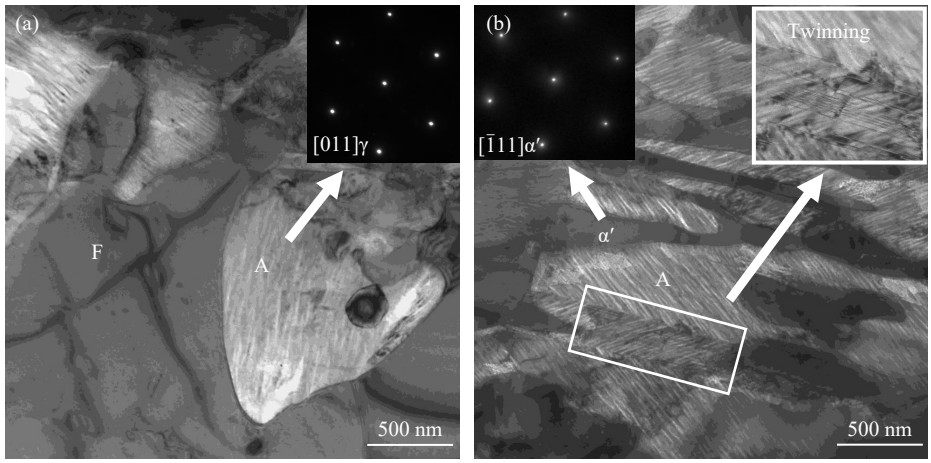

Fig. 8. Bright-field TEM micrographs of undeformed steel: (a) ferrite and small-sized austenite island; (b) large-sized austenite island with twinning and α′-martensite in the interior. (a) Reprinted from *Int. J. Fatigue*, 165, M. Zhang, W.J. Wang, B.D. Zhang, *et al.*, Influence of pre-straining on the low-cycle fatigue performance of Fe–0.1C–5Mn medium manganese steel, 107186, Copyright 2022, with permission from Elsevier.

austenite (Fig. 10(a)). The SAED pattern obtained from the marked region in Fig. 10(a) revealed the hexagonal close-packed structure of ε-martensite within the austenite matrix. As shown in Fig. 10(c), some fresh α′-martensite phases were detected in the interior of large-sized RA islands, which exhibited a higher dislocation density compared with that observed in Fig. 9(b).

4. Discussion

4.1. Lüders band propagation and PLC effect on mechanical properties

The investigated material revealed a yield point elongation of ~1.5%, which is reduced compared with those of other ultra-fine-grained MMnS. The short yield point elongation was assumed to be due to the enlarged grain sizes (2.1 μm for ferrite and 0.8 μm for austenite averagely) achieved through annealing at 625°C for an extended period of 12 h. The DIC measurement indicated the LS fluctuation at the low GS of 1%–3%. The LS was associated with Lüders band propagation throughout the specimens. At the 1% GS, the high-LS region obtained a major strain of 1.2%, and the other regions exhibited considerably lower strains, around 0.5%. During the yield stage, the XRD results indicated the hardly detectable transformation of RA to martensite during the yielding stage. Wang *et al.* [15] reported that martensitic transformation is neither a cause nor a direct influence of Lüders band formation; however, it can accelerate the formation of Lüders band through the rapid generation of dislocations and simultaneous increase in their velocities. Therefore, Lüders band formation was detectable in the low-deformation region and disappeared at 3% GS. In return, the reduction in LS fluctuation also partially suppressed the strain-induced martensitic transformation in the low-strain region.

From the 1% GS to the 20% GS, the material strength increased continuously from 510 to 720 MPa. DIC revealed a homogeneous strain distribution throughout the specimen, except for the occasional small fluctuation caused by localized deformation due to the passing Lüders band at early deformation stages. The XRD measurements indicate a gradual decrease in the volume fraction of the RA from 26.4% to 17.9%. As the GS exceeded 20% (Fig. 3), strain localization at several sites intensified. Accordingly, serrated flow occurred between 18% and 30% GS, as shown by the tensile

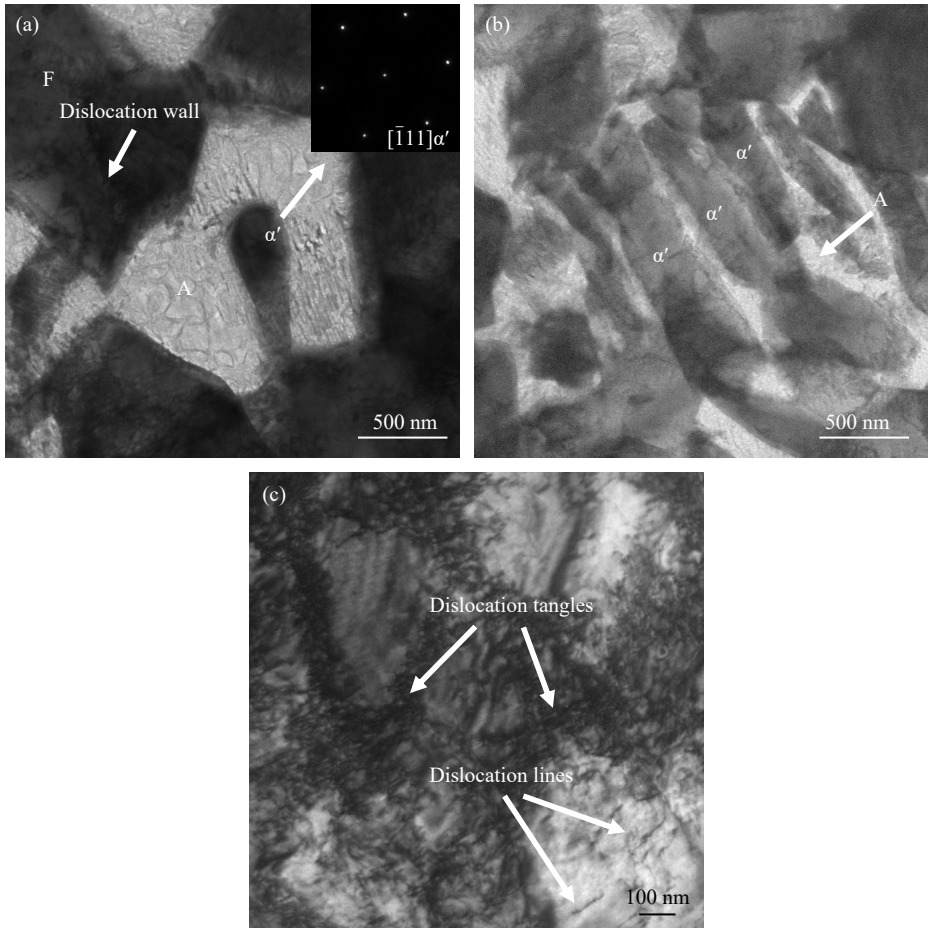

Fig. 9. Bright-field TEM micrographs of Fe–0.1C–5Mn steel with a 10% deformation strain: (a) martensite grain (α′) formed in the interior of a relatively small-sized RA; (b) fresh α′-martensite grains formed in the interior of a large-sized RA; (c) ferrite matrix with a very high dislocation density. (a, b) Reprinted from *Int. J. Fatigue*, 165, M. Zhang, W.J. Wang, B.D. Zhang, *et al.*, Influence of pre-straining on the low-cycle fatigue performance of Fe–0.1 C–5Mn medium manganese steel, 107186, Copyright 2022, with permission from Elsevier.

stress–strain curve in Fig. 1. Continuous TRIP and/or TWIP effects were assumed to occur in conjunction with flow serrations. XRD measurement also revealed a gradual decrease in the volume fraction of RA from 17.9% to 8.2% until the UE ended [31]. The stable and continuous TWIP/TRIP-associated transformation continuously strengthened the material and delayed necking behavior.

Compared with martensite, austenite had a higher carbon solubility. During the austenite-to-martensite transformation processes, the carbon in martensite became supersaturated, which led to volume expansion and a concave–convex appearance of the surface. The decohesion of the ferrite/martensite and ferrite/austenite interfaces, along with the fracture of martensite, was facilitated by the LS incompatibility and low toughness of α′-martensite [32]. The RA can eliminate or reduce stress concentration at the phase boundary/interface through the TRIP effect, which delayed the nucleation, growth, and aggregation of microvoids. As a result, the material's plasticity showed an increase [33].

Fig. 5 illustrates the presence of the RA with high stability and predominantly small-sized austenite island (about 1 μm in length). The Mn content of small-sized RA islands, as confirmed by EDS, was considerably higher than that of large-sized ones (around 2 μm), as presented in Table 1. According to the Hall–Patch equation, the transformation of small-sized RA islands required a large mechanical free energy. The high Mn content effectively improved the stability of RA, which indicates the considerably higher stability of small-sized RA compared with large-sized ones [12,34].

The austenite transformation trend was predicted using Eq. (2), as shown in Fig. 7(b). The fitting of the transformation equation $f_\gamma = 0.268\exp(-2.91\varepsilon)$ indicates f_0 and k of 0.268 and 2.91, respectively. However, as mentioned in Section 3.2, different sizes of RA contain different Mn contents, which show different stabilities. More in-depth investigations on the transformation kinetics of austenite with different features must be conducted.

4.2. Microstructural evolution during tensile deformation

The evolution of microstructure is presented in Figs. 8–10. Sparse dislocations were observed in ferrite, and thermal martensite was formed during the cooling process of heat treatment (Fig. 8). The lath-like martensite allowed dislocation movement and dislocation cell formation, which contributed to the suppression of Lüders bands [31]. The intro-

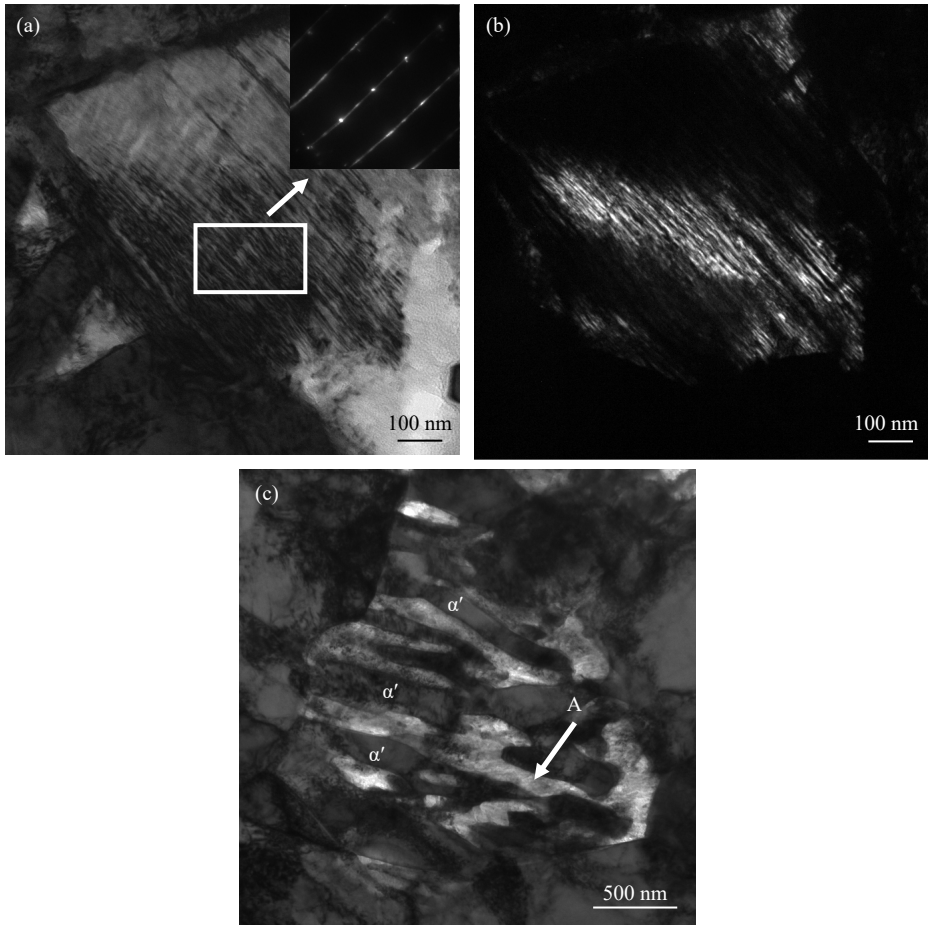

Fig. 10. TEM micrographs of Fe–0.1C–5Mn steel with a 30% deformation strain: (a) bright-field image showing high planar faults and ε-martensite grains; (b) dark-field image revealing planar faults; (c) large-sized RA island with a partially transformed fresh α′-martensite phase in the interior of austenite.

Table 1. Size and Mn content of different phases measured in Fig. 5(a)

Grain	Size / μm	Mn / wt%
Large-sized austenite	2.5	7.5
Small-sized austenite	0.8	10.0
Ferrite	2.1	2.5

duction of lath-like martensite in large-sized austenite islands possibly caused a reduction in the yield point elongation in the investigated material. After 10% deformation, lath-like martensite was introduced to some large-sized austenite islands with low stability. Some small-sized austenite islands remained unchanged after fracture, which indicates their high stability. Furthermore, the crystallographic relationship between large-sized austenite grains with a zone axis [011] and their neighbor ferrite grains with a zone axis [$\bar{1}$11] followed the Kurdjumov–Sachs orientation relationship, i.e., $<\bar{1}11>_{\alpha'}//<011>_{\gamma}$ and $\{011\}_{\alpha'}//\{111\}_{\gamma}$, after IA, as proven by the SAED pattern [26]. Dislocations in martensite increased considerably after tensile deformation compared with those in the undeformed martensite (Figs. 8 and 10), which improved material strength.

Combined with the XRD findings presented in Fig. 7, the presence of thin parallel ε-martensite plates in large-sized austenite surrounded by SFs was demonstrated (Fig. 10(a)), which transformed further to α′-martensite. The transformation was verified by the presence of SFs in Fig. 10. The formation of α′-martensite requires the intersection of microscopic shear bands, such as SFs and ε-martensite plates [35]. No evident SFs and ε-martensite were observed in small-sized austenite grains.

The primary deformation mechanisms during the tensile process of small-sized austenite grains included the dislocation slip and martensitic transformation. PLC bands expended stably and continuously due to the small grain size of austenite. The occurrence of the PLC band depended on the size of RA and sufficient dislocations that it generated [17]. A progressive transformation occurred during tension because of the high stability of the small-sized RA, which actively contributed to the mechanical properties of the test steel.

Fig. 11 illustrates the schematic of the microstructural evolution and the crack initiation mechanisms of the investigated steel during the uniaxial tensile test. The austenite was categorized into large-sized and small-sized grains, with a small amount of lath martensite present in large-sized grains. The stability of large-sized austenite was substantially lower than that of small-sized ones. The transformation of large-sized austenite to martensite mainly occurred from the end of

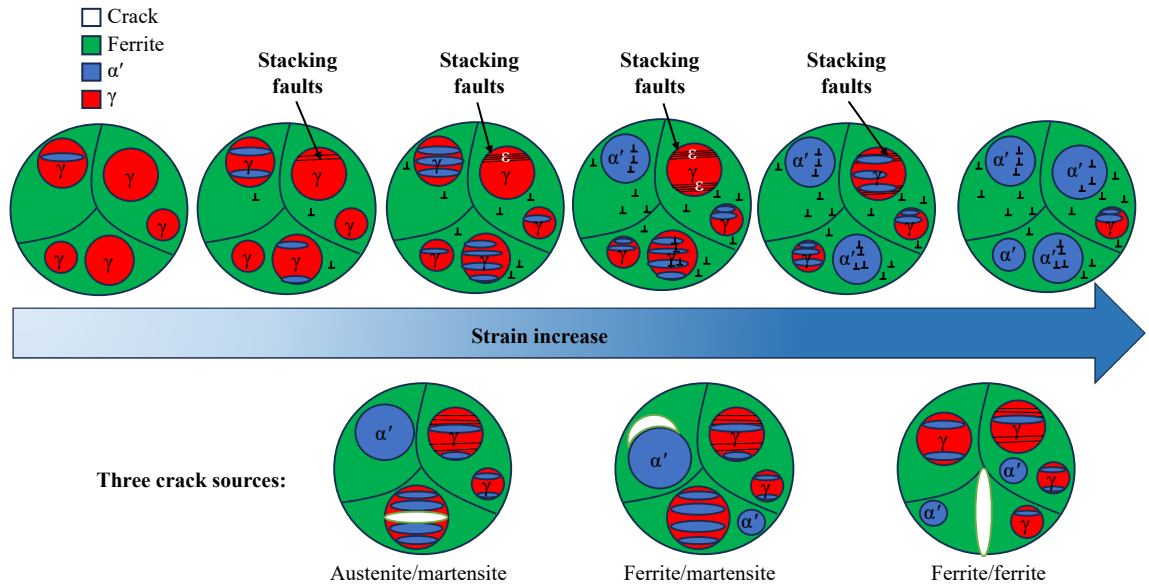

Fig. 11. Schematic of austenite to martensitic transformation behaviors and the potential crack initiation sites during the tensile process.

yield to 20% strain. Consequently, this phenomenon had minimal influence on the extension of yield point and improved the mechanical stability of materials. SFs and ε-martensite were observed in some large-sized austenite, and the small-sized austenite endured less martensitic transformation. In the late deformation stage, fracture initiation primarily occurred at the austenite/martensite and ferrite/martensite interfaces and inside the ferrite phase.

The matrix of Fe–0.1C–5Mn steel consisted of ferrite grains (Fig. 5), and the second phase was RA, whose grain size was generally smaller than ferrite. The deformation of the steel before the GS of 20% was dominated by the ferrite phase, supplemented by a small amount of martensitic transformation. The deformation energy is distributed uniformly in most ferrite grains. Strain localization occurred when the GS exceeded 20%, which was partly due to the discontinuous TRIP/TWIP effects caused by the large-sized RA in steel. However, the fresh α′-martensite phase transformed from the RA did not further deform during subsequent straining due to its high strength, which resulted in dislocation plugging. As a result, the large-sized RA transformed into martensite, and some small-sized austenite with a considerably higher Mn content remained unchanged.

5. Conclusions

This work investigated a cold-rolled Fe–0.1C–5Mn steel, which exhibited progressive TRIP effect with limited Lüders band and stable mechanical properties during tensile deformation. The relationship among structures, mechanical properties, microstructure transformation, and deformation mechanisms was explored systematically during the tensile process. The following conclusions were obtained.

(1) The investigated Fe–0.1C–5Mn steel exhibited an excellent combination of UTS of 775 MPa and TE of around 40% and UTS × TE of 31 GPa·%.

(2) The Lüders strain was limited to ~1.5%, which was attributed to the suppressed martensitic transformation during the yielding stage. The large-sized RA was less stable and transformed to α′-martensite during the initial uniform plastic deformation stage. SFs and ε-martensite were detected in several large-sized RA. From a strain level of 20%–30%, small-sized RA gradually transformed to martensite, which enabled the stable and continuous expansion of PLC bands.

(3) Martensitic transformation did not occur in some ultrafine small-sized RA unless considerably large strains had been reached. The crack initiation sites were primarily austenite/martensite and ferrite/martensite interfaces or inside ferrites.

Acknowledgement

This work was financially supported by the National Key R&D Program of China (No. 2017YFB0304402).

Conflict of Interest

Han Dong is an editorial board member for this journal and was not involved in the editorial review or the decision to publish this article. On behalf of all authors, the corresponding authors state that there is no conflict of interest.

References

[1] S.S. Li and H.W. Luo, Medium-Mn steels for hot forming application in the automotive industry, *Int. J. Miner. Metall. Mater.*, 28(2021), No. 5, p. 741.

[2] H. Xu, L.J. Zhou, W.L. Wang, and Y. Yi, A simple route for preparation of TRIP-assisted Si–Mn steel with excellent performance using direct strip casting, *Int. J. Miner. Metall. Mater.*, 31(2024), No. 10, p. 2173.

[3] B. Hu, H. Sui, Q.H. Wen, Z. Wang, A. Gramlich, and H.W. Luo, Review on the plastic instability of medium-Mn steels for identifying the formation mechanisms of Lüders and Portevin–

Le Chatelier bands, *Int. J. Miner. Metall. Mater.*, 31(2024), No. 6, p. 1285.
[4] Y. Ma, R. Zheng, Z.Y. Gao, *et al*., Multiphase-field simulation of austenite reversion in medium-Mn steels, *Int. J. Miner. Metall. Mater.*, 28(2021), No. 5, p. 847.
[5] M.T. Kim, T.M. Park, K.H. Baik, W.S. Choi, and J. Han, Effects of cold rolling reduction ratio on microstructures and tensile properties of intercritically annealed medium-Mn steels, *Mater. Sci. Eng. A*, 752(2019), p. 43.
[6] W.Q. Cao, C. Wang, J. Shi, M.Q. Wang, W.J. Hui, and H. Dong, Microstructure and mechanical properties of Fe–0.2C–5Mn steel processed by ART-annealing, *Mater. Sci. Eng. A*, 528(2011), No. 22-23, p. 6661.
[7] M.H. Cai, W.J. Zhu, N. Stanford, L.B. Pan, Q. Chao, and P.D. Hodgson, Dependence of deformation behavior on grain size and strain rate in an ultrahigh strength-ductile Mn-based TRIP alloy, *Mater. Sci. Eng. A*, 653(2016), p. 35.
[8] S. Lee and B.C. De Cooman, Annealing temperature dependence of the tensile behavior of 10 pct Mn multi-phase TWIP-TRIP steel, *Metall. Mater. Trans. A*, 45(2014), No. 13, p. 6039.
[9] Y.J. Wang, S. Zhao, R.B. Song, and B. Hu, Hot ductility behavior of a Fe–0.3C–9Mn–2Al medium Mn steel, *Int. J. Miner. Metall. Mater.*, 28(2021), No. 3, p. 422.
[10] S.P. Neog, A. Lodh, A. Karmakar, *et al*., Insights into the stability of retained austenite during wear, *Philos. Mag.*, 103(2023), No. 3, p. 203.
[11] M.J. Zhao, L.H. Jiang, C.M. Li, L. Huang, C.Y. Sun, J.J. Li, and Z.H. Guo, Flow characteristics and hot workability of a typical low-alloy high-strength steel during multi-pass deformation, *Int. J. Miner. Metall. Mater.*, 31(2024), No. 2, p. 323.
[12] J. Hu, X.Y. Li, Q.W. Meng, L.Y. Wang, Y.Z. Li, and W. Xu, Tailoring retained austenite and mechanical property improvement in Al–Si–V containing medium Mn steel via direct intercritical rolling, *Mater. Sci. Eng. A*, 855(2022), art. No. 143904.
[13] X.G. Wang and M.X. Huang, Temperature dependence of Lüders strain and its correlation with martensitic transformation in a medium Mn transformation-induced plasticity steel, *J. Iron Steel Res. Int.*, 24(2017), No. 11, p. 1073.
[14] M. Callahan, O. Hubert, F. Hild, A. Perlade, and J.H. Schmitt, Coincidence of strain-induced TRIP and propagative PLC bands in medium Mn steels, *Mater. Sci. Eng. A*, 704(2017), p. 391.
[15] W.Q. Liu and J.H. Lian, Stress-state dependence of dynamic strain aging: Thermal hardening and blue brittleness, *Int. J. Miner. Metall. Mater.*, 28(2021), No. 5, p. 854.
[16] B.H. Sun, N. Vanderesse, F. Fazeli, *et al*., Discontinuous strain-induced martensite transformation related to the Portevin–Le Chatelier effect in a medium manganese steel, *Scripta Mater.*, 133(2017), p. 9.
[17] F. Yang, H.W. Luo, E.X. Pu, S.L. Zhang, and H. Dong, On the characteristics of Portevin–Le Chatelier bands in cold-rolled 7Mn steel showing transformation-induced plasticity, *Int. J. Plast.*, 103(2018), p. 188.
[18] L.P. Tang, P.F. Wei, Z.L. Hu, and Q. Pang, Microstructure and mechanical properties stability of pre-hardening treatment in Al–Cu alloys for pre-hardening forming process, *Int. J. Miner. Metall. Mater.*, 31(2024), No. 3, p. 539.
[19] F. Yang, J. Zhou, Y. Han, P. Liu, H.W. Luo, and H. Dong, A novel cold-rolled medium Mn steel with an ultra-high product of tensile strength and elongation, *Mater. Lett.*, 258(2020), art. No. 126804.
[20] S. Yan, T.L. Li, T.S. Liang, J.Q. Chen, Y. Zhao, and X.H. Liu, By controlling recrystallization degree: A plain medium Mn steel overcoming Lüders deformation and low yield-to-tensile ratio simultaneously, *Mater. Sci. Eng. A*, 758(2019), p. 79.
[21] H.S. Wang, Y.X. Zhang, G. Yuan, *et al*., Significance of cold rolling reduction on Lüders band formation and mechanical behavior in cold-rolled intercritically annealed medium-Mn steel, *Mater. Sci. Eng. A*, 737(2018), p. 176.
[22] Z.C. Li, H. Ding, R.D.K. Misra, and Z.H. Cai, Deformation behavior in cold-rolled medium-manganese TRIP steel and effect of pre-strain on the Lüders bands, *Mater. Sci. Eng. A*, 679(2017), p. 230.
[23] J. Wu, Y. Hovanski, and M. Miles, Digital image correlation characterization and formability analysis of aluminum alloy TWB during forming, *Materials*, 15(2022), No. 15, art. No. 5291.
[24] T. Wang, J. Hu, and R.D.K. Misra, Microstructure evolution and strain behavior of a medium Mn TRIP/TWIP steel for excellent combination of strength and ductility, *Mater. Sci. Eng. A*, 753(2019), p. 99.
[25] B.H. Sun, F. Fazeli, C. Scott, N. Brodusch, R. Gauvin, and S. Yue, The influence of silicon additions on the deformation behavior of austenite–ferrite duplex medium manganese steels, *Acta Mater.*, 148(2018), p. 249.
[26] P.J. Gibbs, E. De Moor, M.J. Merwin, B. Clausen, J.G. Speer, and D.K. Matlock, Austenite stability effects on tensile behavior of manganese-enriched-austenite transformation-induced plasticity steel, *Metall. Mater. Trans. A*, 42(2011), No. 12, p. 3691.
[27] C. Wang, W.Q. Cao, J. Shi, C.X. Huang, and H. Dong, Deformation microstructures and strengthening mechanisms of an ultrafine grained duplex medium-Mn steel, *Mater. Sci. Eng. A*, 562(2013), p. 89.
[28] X.G. Wang, L. Wang, and M.X. Huang, Kinematic and thermal characteristics of Lüders and Portevin–Le Châtelier bands in a medium Mn transformation-induced plasticity steel, *Acta Mater.*, 124(2017), p. 17.
[29] E.J. Seo, J.K. Kim, L. Cho, J. Mola, C.Y. Oh, and B.C. De Cooman, Micro-plasticity of medium Mn austenitic steel: Perfect dislocation plasticity and deformation twinning, *Acta Mater.*, 135(2017), p. 112.
[30] M. Zhang, W.J. Wang, B.D. Zhang, Q.Y. Cen, and J. Liu, Influence of pre-straining on the low-cycle fatigue performance of Fe–0.1C–5Mn medium manganese steel, *Int. J. Fatigue*, 165(2022), art. No. 107186.
[31] K. Steineder, D. Krizan, R. Schneider, C. Béal, and C. Sommitsch, On the microstructural characteristics influencing the yielding behavior of ultra-fine grained medium-Mn steels, *Acta Mater.*, 139(2017), p. 39.
[32] B.H. Sun, D. Palanisamy, D. Ponge, *et al*., Revealing fracture mechanisms of medium manganese steels with and without delta-ferrite, *Acta Mater.*, 164(2019), p. 683.
[33] B.V. Narasimha Rao and G. Thomas, Structure-property relations and the design of Fe-4Cr-C base structural steels for high strength and toughness, *Metall. Trans. A*, 11(1980), No. 3, p. 441.
[34] E. De Moor, D.K. Matlock, J.G. Speer, and M.J. Merwin, Austenite stabilization through manganese enrichment, *Scripta Mater.*, 64(2011), No. 2, p. 185.
[35] J. Talonen, H. Hänninen, P. Nenonen, and G. Pape, Effect of strain rate on the strain-induced $\gamma \rightarrow \alpha'$-martensite transformation and mechanical properties of austenitic stainless steels, *Metall. Mater. Trans. A*, 36(2005), No. 2, p. 421.